Computer-aided diagnostic scheme for the detection of lung nodules on chest radiographs: Localized search method based on anatomical classification

Junji Shiraishi,[a)] Qiang Li, Kenji Suzuki, Roger Engelmann, and Kunio Doi
Kurt Rossmann Laboratories for Radiologic Image Research, Department of Radiology,
The University of Chicago, 5841 S. Maryland Avenue, MC 2026, Chicago, Illinois 60637

We developed an advanced computer-aided diagnostic (CAD) scheme for the detection of various types of lung nodules on chest radiographs intended for implementation in clinical situations. We used 924 digitized chest images (992 noncalcified nodules) which had a 500×500 matrix size with a 1024 gray scale. The images were divided randomly into two sets which were used for training and testing of the computerized scheme. In this scheme, the lung field was first segmented by use of a ribcage detection technique, and then a large search area (448×448 matrix size) within the chest image was automatically determined by taking into account the locations of a midline and a top edge of the segmented ribcage. In order to detect lung nodule candidates based on a localized search method, we divided the entire search area into 7×7 regions of interest (ROIs: 64×64 matrix size). In the next step, each ROI was classified anatomically into apical, peripheral, hilar, and diaphragm/heart regions by use of its image features. Identification of lung nodule candidates and extraction of image features were applied for each localized region (128×128 matrix size), each having its central part (64×64 matrix size) located at a position corresponding to a ROI that was classified anatomically in the previous step. Initial candidates were identified by use of the nodule-enhanced image obtained with the average radial-gradient filtering technique, in which the filter size was varied adaptively depending on the location and the anatomical classification of the ROI. We extracted 57 image features from the original and nodule-enhanced images based on geometric, gray-level, background structure, and edge-gradient features. In addition, 14 image features were obtained from the corresponding locations in the contralateral subtraction image. A total of 71 image features were employed for three sequential artificial neural networks (ANNs) in order to reduce the number of false-positive candidates. All parameters for ANNs, i.e., the number of iterations, slope of sigmoid functions, learning rate, and threshold values for removing the false positives, were determined automatically by use of a bootstrap technique with training cases. We employed four different combinations of training and test image data sets which was selected randomly from the 924 cases. By use of our localized search method based on anatomical classification, the average sensitivity was increased to 92.5% with 59.3 false positives per image at the level of initial detection for four different sets of test cases, whereas our previous technique achieved an 82.8% of sensitivity with 56.8 false positives per image. The computer performance in the final step obtained from four different data sets indicated that the average sensitivity in detecting lung nodules was 70.1% with 5.0 false positives per image for testing cases and 70.4% sensitivity with 4.2 false positives per image for training cases. The advanced CAD scheme involving the localized search method with anatomical classification provided improved detection of pulmonary nodules on chest radiographs for 924 lung nodule cases. © *2006 American Association of Physicists in Medicine*. [DOI: 10.1118/1.2208739]

I. INTRODUCTION

Lung cancer has been the leading cause of cancer death in the United States since 1987, and is expected to comprise 28% of all cancers in 2004.[1] Therefore, several projects, including screening by use of low-dose helical CT scans and chest radiography, have been attempted[2,3] and are currently being evaluated[4,5] in order to improve the rate of early detection of lung cancer. In the detection of lung cancer at an early stage, screening by CT is clearly superior to screening by chest radiographs;[4] however, there are some issues with CT screening such as a large number of false-positive (benign nodule) findings and overdiagnosis. Therefore, the use of CT screening for lung cancer is a highly controversial issue at present.[6]

Chest radiography, which is simple to perform and inexpensive, has been used as the first and most common examination even when this examination was done for purposes other than lung cancer detection. It should be noted that the large number of chest radiography examinations compared to

thoracic CT scans indicates that there are many more opportunities to detect lung abnormalities in the community by use of chest radiographs than by use of CT examinations. For example, an average annual number of 236 chest radiography examinations were obtained per 1000 population compared with 19 body CT scans for the same patient group in the same period, between 1991 and 1996.[7] Therefore, if we could assume empirically that thoracic CT would account for 25% of all body CT scans, then there would be 50 times as many opportunities to detect lung nodules with chest radiography as with thoracic CT. However, it has been well demonstrated that detection of lung cancer at an early stage on chest radiographs is a very difficult task for radiologists.[8–11]

Since the early 1980s, the concept of and the methodology for computer-aided diagnosis (CAD) have been developed to assist radiologists in detecting lesions and improving their sensitivity in the differential diagnosis. Unlike the concept of an automated diagnostic system which was proposed in the 1960s, CAD may be defined generally as a diagnosis made by a radiologist who takes into account the results of automated computer analysis of radiologic images.[12,13] Therefore, the computer output may be used as a "second opinion" for improving radiologists' decision-making and avoiding oversight, but it should not be used independently without physicians' judgment.

The development of a CAD scheme for detection of lung nodules in chest radiographs has been one of the important projects in our laboratory among CAD methods for various radiologic modalities.[14–17] In addition, several approaches to the detection of lung nodules on chest radiographs were reported by Suzuki et al.,[18] Lo et al.,[19] Mao et al.,[20] and Penedo et al.[21] Although the performance of the CAD scheme for detection of lung nodules has achieved a relatively modest sensitivity, with a small number of false positives per image, such as sensitivities of 73.3% with 0.76 false positive per image by Suzuki et al.,[18] and 70.0% with 1.7 false positives per image by Xu et al.,[17] it is important to note that this level of performance was realized with only a small number of cases.

The first commercial system for lung nodule detection CAD was developed by Deus Technology Inc. (Riverain Medical at present) and received FDA approval for clinical use in 2001. With this commercial CAD system, Freedman et al.[22] reported a sensitivity of 65.0% with 5.3 false positives per image from a clinical trial in an independent validation test by use of 80 cases containing small primary lung cancers and 160 cases not containing cancers. Kakeda et al.[23] reported the use of another commercial CAD system developed by Mitsubishi Space Software for the detection of lung nodules: the performance of this CAD system indicated a sensitivity of 73.0% with 4.0 false positives per image for 274 chest radiographs including 323 lung nodules.

As mentioned earlier, the performance of CAD schemes for the detection of lung nodules depends strongly on the number of cases and the characteristics of the image database used for their development. For example, the smaller the number of cases used for training of a CAD scheme, the lower the performance for testing new different cases would

be. Therefore, when the number of cases used in the study would become sufficiently large, we may assume that the performance of a CAD scheme for lung nodule detection could be estimated in actual clinical situations.

In this study, we developed an advanced computerized scheme for the detection of lung nodules on chest radiographs by use of a large number of cases including 924 chest images with 992 lung nodules. This advanced method was developed by incorporating several new techniques, including a localized search method, an adaptive image filter applied to the anatomical classification for a localized region, a contralateral subtraction technique, as well as automated parameter settings for artificial neural networks (ANNs) by use of four different combinations of training and test data sets which were randomly selected from the original image database.

II. MATERIAL AND METHODS

A. Image database

We initially collected a total number of 1000 lung nodule cases (1076 lung nodules) for this study, which included 411 screen-film chest radiographs and 589 digital chest images. Digital chest images were collected at two institutions in the United States and three institutions in Japan. Screen-film images were obtained from two institutions in the United States and one institution in Taipei, Republic of China, and then digitized by use of a laser film digitizer. One hundred fifty-four nodule cases in the Japanese Standard Digital Image Database developed by the Japanese Society of Radiological Technology,[24] which is publicly available, were also included. All nodules were confirmed initially by CT examination and/or the consensus of radiologists at each institution. Genders in this database were 376 females, 391 males, and 233 unknown.

The criteria for nodule cases to be included in the 1000-image database were: (1) "actionable" cases[25] with nodules in which radiologists can identify their locations correctly, (2) nodule margins which can be confirmed by radiologists on chest images, (3) no repeat cases from the same patient, (4) no suspicious nodules which were not confirmed by CT examination, (5) no cases with other major abnormalities which might affect radiologists' decision-making for the detection of nodules, (6) no cases with poor-quality images such as extremely low exposure in digital images and films, and (7) 60 mm for the maximum nodule size, but no "very obvious" nodules larger than 40 mm. In addition, 76 chest images (84 lung nodules) in the 1000 chest images were excluded because these images included lung nodules located in opaque areas of the chest image, i.e., the mediastinum, retrocardiac lung, and lung projected on or below diaphragm (subdiaphragmatic lung) regions. Please note that we used the term "opaque area" for indicating one specific area which included the mediastinum, retrocardiac lung, and lung projected below or on diaphragm regions, in order to distinguish these regions from the projected lung fields which were the subject of this study. Finally, we used 924 chest images including 992 lung nodules in this study for the train-

TABLE I. The number of lung nodules in each subtlety group and in each nodule size group for 924 lung nodule cases.

Degree of subtlety	Effective diameter of lung nodules (mm)						Total
	5–10	10–15	15–20	20–25	25–30	30–40	
Extremely subtle	4	13	18	14	2	2	53(5.3%)
Very subtle	16	63	63	40	22	4	208(21.0%)
Subtle	30	131	111	97	43	14	426(42.9%)
Relatively obvious	21	82	62	48	21	6	240(24.2%)
Obvious	5	23	19	15	3	0	65(6.6%)
Total	76	312	273	214	91	26	992
	(7.7%)	(31.5%)	(27.5%)	(21.6%)	(9.2%)	(2.6%)	

ing and testing of the CAD scheme. Because the original chest images had various combinations of matrix size, pixel size, and gray scales, all of the images were converted to a 500×500 matrix size (0.7 mm pixel size) and 10 bit gray scale by use of an averaging subsampling method and a bit-shift method. In addition, the gray level and contrast of all images were optimized manually by one co-author (J.S.) in order to correct for inadequate exposure conditions.

In order to determine the size of lung nodules and the degree of subtlety for radiologists' visual detection of lung nodules, we obtained manual outlines of nodules (for size) and five-scale subjective ratings (for subtlety) by the consensus of three radiologists. The five degrees of subtlety in the detection of a lung nodule were defined as extremely subtle, very subtle, subtle, relatively obvious, and obvious. Table I shows the number of cases in each subtlety group and each size group of lung nodules for all 992 lung nodules, where the effective diameter was determined by the diameter of the circle that had the same area as that of the nodule outline.[14] The numbers of lung nodules in the database were 53 extremely subtle, 208 very subtle, 426 subtle, 240 relatively obvious, and 65 obvious, and the mean size was 17.6 mm (size range, 6.0–37.9 mm).

First, we divided the 1000 cases randomly into 500 training and 500 test cases, and we then eliminated 76 cases including 84 lung nodules located in opaque areas, as described earlier. Therefore, we had 465 training cases (500 lung nodules) and 459 test cases (492 lung nodules) in the first data-set partition. We used training cases only for the development of the computerized scheme, such as selection of image features, determination of threshold values, and parameter settings for ANNs such as the number of iterations, slope of sigmoid functions, learning rate, and threshold values for removing false positives. Test cases were used for validating the performance of the computerized scheme trained with the training cases. In this study, we repeated the same procedure of training and testing four times with four different combinations of disjoint training and test cases. In order to create four different combinations, we obtained two different sets of training and testing cases first, and then we switched training cases and test cases in each set. The number of cases in each subgroup discussed in the following indicates the numbers obtained from the first set of training

and test cases; therefore, slightly different numbers of cases were used in the four combinations, as shown later.

B. Computerized scheme for nodule detection

As shown in Fig. 1, our new CAD scheme for the detection of lung nodules consists of three major steps, i.e., (1) segmentation of lung fields and anatomical classification by 7×7 regions of interest (ROIs), (2) identification of initial nodule candidates and extraction of image features in the original, density-trend-corrected original, nodule-enhanced, and contralateral subtraction images,[26] and (3) elimination of false positives by use of sequential application of three ANNs for the distinction between true positive and false-
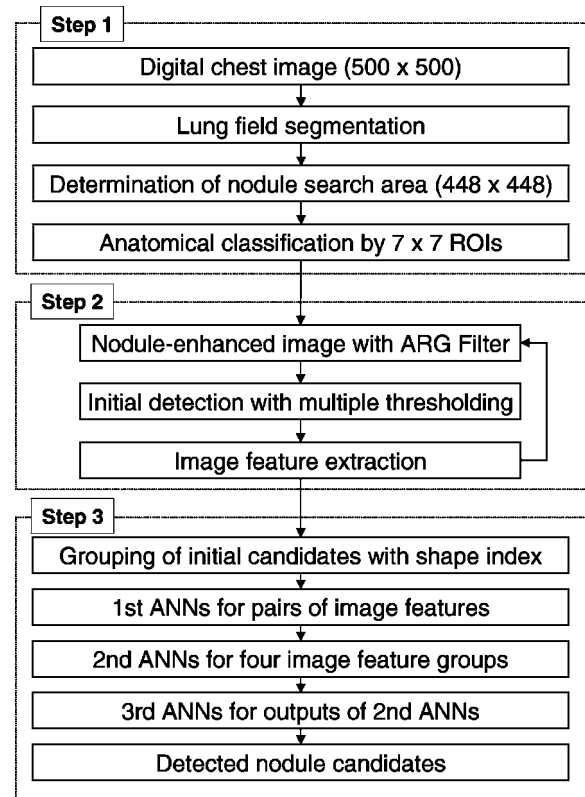

FIG. 1. Overall computerized scheme for the detection of lung nodules on chest images.
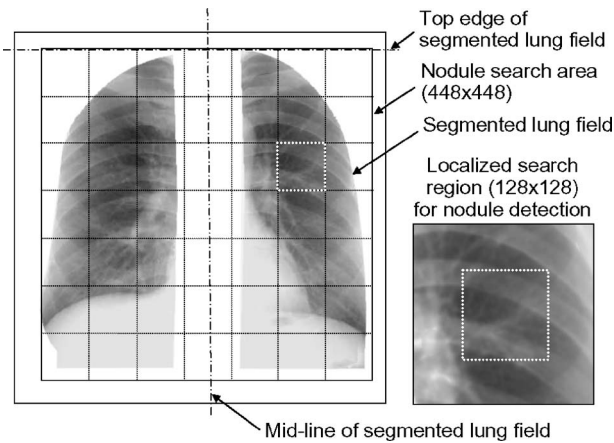
FIG. 2. Example of segmented lung field and 7×7 matrixes of ROIs adjusted to the midline and top edge of the segmented lung field. The ROI has 128×128 matrix size which covers an entire lung field by overlapping two ROIs.

FIG. 3. Example of anatomical classification for 7×7 matrixes of ROIs which were determined by use of the location of ROI, an average and standard deviation of pixel values, and the histogram of the edge gradient in each ROI.

positive candidates. In these three steps, we introduced several new techniques into our existing computerized scheme, such as grouping of nodule candidates in different anatomical regions for all of the subsequent steps, the low-pass filter technique in step 1, an average radial gradient (ARG) filtering technique for the initial detection, and extraction of new image features in contralateral subtraction images in step 2, and an automated method for determining parameter settings for a sequential application of three ANNs in step 3. Details of our computerized scheme are described in the following.

1. Segmentation of lung fields and classification of anatomical regions

Before the segmentation of lung fields, we applied a low-pass filter technique to the input original image in order to remove the effect of edge enhancement by the unsharp masking technique.

The entire lung region, including the mediastinum, retrocardiac lung, and subdiaphragmatic lung, was segmented initially by use of ribcage edge detection techniques.[27,28] Once we had segmented the lung field, a nodule search area (448×448 matrix size) including 49 (7×7) ROIs (64×64 matrix size) was placed over the original image. The location of nodule-search area was determined based on the locations of a midline and top-edge of the segmented lung field as illustrated in Fig. 2. Each ROI in the nodule search area was classified automatically into four different anatomical regions, i.e., (1) apical, (2) peripheral, (3) hilum, and (4) opaque areas and outside the boundary of lung fields. In the anatomical classification, the location of the ROI was used first. Figure 3 illustrates an example of anatomical segmentations for the same case as shown in Fig. 2. In this classification, the ROIs located in the upper two rows in 7×7 matrixes are likely to be classified as "apical" regions, and the ROIs located in the middle three columns are likely to be classified as "hilum" region. In addition, an average pixel value and the histogram of the edge gradient in each ROI were used for distinguishing peripheral regions of the lung
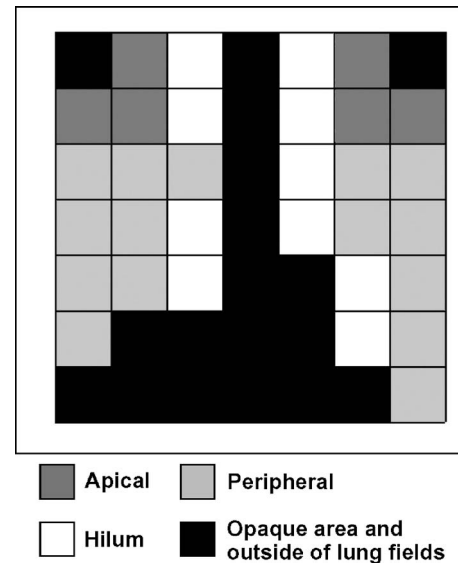
field from the apical and hilum regions. For example, the ROI located in peripheral region was likely to have strong edge gradients in two orthogonal directions due to anterior and posterior rib edges, and also to have relatively low pixel values (i.e., low densities) compared with the ROI in the hilum region. The next step for identifying nodule candidates was executed only when the corresponding ROI was classified as apical, peripheral, or hilum regions, because an opaque area was not a subject of this study.

The localized search regions for identifying nodule candidates had a 128×128 matrix size, each region having its central part (64×64 matrix size) located at a position corresponding to ROI which was classified anatomically in the previous step as shown in Fig. 2. Therefore, a localized search region was overlapped with adjacent ones on the original image. In addition to the original image, the density-trend-corrected image for the original image was processed in each localized region by use of a two-dimensional density trend correction technique[29] together with a Gaussian smoothing filter. Because of the density trends that were caused by differences in body thickness, especially near the chest wall, it was very difficult to isolate lung nodules attached to the chest wall without density trend corrections.

2. Identification of initial nodule candidates and extraction of image features

A nodule-enhanced image was obtained from the density-trend corrected image for each localized search region in order to identify initial nodule candidates in the subsequent step. The nodule-enhanced image was provided by sequential application of the ARG filter and the Gaussian filter that were obtained from the density-trend-corrected image. Figure 4 illustrates the ARG filter. The radial component of the local edge gradient at the pixel $P(i,j)$ toward the pixel
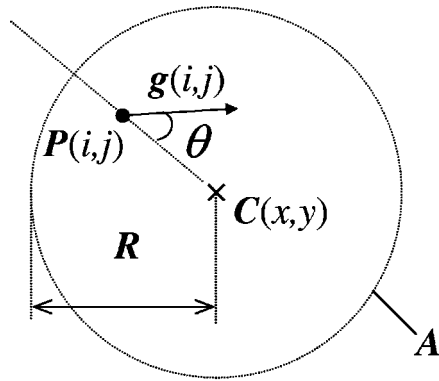
$$\mathbf{ARG}(x,y) = \frac{1}{|A|} \sum_{(i,j) \in A} |g(i,j)| \cos \theta$$

$g(i,j)$: edge gradient at (i,j)

$|A|$: area of the circle A (radius = R)

FIG. 4. Explanation of the average radial gradient (ARG) filtering technique for a calculation point $C(x,y)$. The ARG filter output $\mathrm{ARG}(x,y)$ was defined as an average value of the radial gradient component of the edge gradient toward the center point at all locations $P(i,j)$ within a circle A (radius = R).

$C(x,y)$ of interest was determined by the magnitude of edge gradient $\mathbf{g}(i,j)$ and the angle between the radial direction and the orientation of the edge gradient. Then, the output of the ARG filter $\mathrm{ARG}(x,y)$ at the pixel $C(x,y)$ was defined as

$$\mathrm{ARG}(x,y) = \frac{1}{|A|} \sum_{(i,j) \in A} |\mathbf{g}(i,j)| \cos \theta, \qquad (1)$$

where $|A|$ is the area of a circle A for the ARG filter that was covered by a radius R,

$$|A| = \{(i,j) | (x-i)^2 + (y-j)^2 < R^2\}. \qquad (2)$$

Because the ARG filter can enhance any regions where edge gradients were oriented toward the center of a circle, low-contrast and/or subtle nodule candidates could be enhanced. In addition, most of the rib edges were not enhanced by this filter, because the gradient of rib edges was not likely to be oriented toward the center of a circle. It is our experience in studies on the detection of lung nodules that the size of lung nodules tends to be large when the location of a nodule is close to the mediastinum region. Therefore, we applied different sizes (ranging from 10.5 to 19.0 mm) of the ARG filter, which was equal to $2R$, depending on the location and the anatomical regions of the ROI.

Multiple-gray-level thresholding of the filtered image was performed for identifying initial nodule candidates. We automatically determined threshold pixel values in each step of thresholding by use of histogram of pixel values within each ROI. We used the area under the histogram, the percentage of which ranged from 0.3% to 60% at high pixel values. Threshold pixel value in each step started from the pixel value corresponding to 0.3% of the area under the histogram, and the subsequent threshold values were determined adaptively by use of 1% of the difference in the area under the

histogram from the previous step. However, if the difference between the two successive threshold values was less than a specific pixel value (1% of the range of the histogram), the threshold value was determined by subtracting the specific pixel value from the previous threshold value. Therefore, the numbers of thresholding and threshold pixel values for each ROI were determined automatically and independently. In addition, multiple-thresholding was completed when the number of identified candidates reached a specific number (i.e., 6 for apical and hilum, and 10 for peripheral), so that the number of thresholding was different in different ROIs.

Initial nodule candidates, which is called an island here and is derived by multiple-gray-level thresholding, were identified if the three image features, i.e., the effective diameter, circularity, and irregularity of a candidate meet the following requirements: an effective diameter[14] of 7.0 mm or greater, circularity[14] of 0.70 or greater, and irregularity[14] of 0.30 or lower for the apical and peripheral regions. These threshold values have been determined empirically during the last two decades. In the initial identification, we monitored the location of centroid of candidate as well as three image features listed earlier. When the three image features of identified candidates were in the range specified for the initial identification; and also the distance between the location of identified candidate and any locations of previously identified candidates was less than two times the effective diameter of identified candidate, all of the features were updated for a newly identified candidate.

In the process of initial identification, we obtained 10 image features based on the contour of an isolated island on the nodule-enhanced image, such as the (1) threshold value [%] at the initial identification level, (2) effective diameter, (3) circularity, (4) irregularity, (5) average pixel value within the island, (6) contrast value obtained by the difference between the maximum and minimum pixel values within the island, (7) normalized horizontal location, (8) normalized vertical location, (9) horizontal distance from the midline, and (10) sequential order of a candidate among all of the candidates detected initially.

In addition to the 10 initial image features, 47 image features were extracted from original, density-trend-corrected original, and nodule-enhanced images at the location of initial detection of a nodule candidate based on geometric features,[14] gray-level features, edge-gradient features[17] and background features which were determined with image features related to the characteristics of the background structure of a nodule candidate. In order to extract some of the image features, we applied two contours of a nodule candidate which were obtained from the density-trend-corrected original and nodule-enhanced images, respectively, by use of the region-growing technique.[30,31] Furthermore, 14 image features were obtained from the corresponding locations of the contralateral subtraction images.[26] Figure 5 illustrates (a) an original image with a nodule candidate indicated by an arrow, and (b) a contralateral subtraction image, together with four small ROIs (50×50 matrix size) which were obtained from (c) original, (d) density-trend corrected original, (e) nodule-enhanced, and (f) contralateral subtraction im-
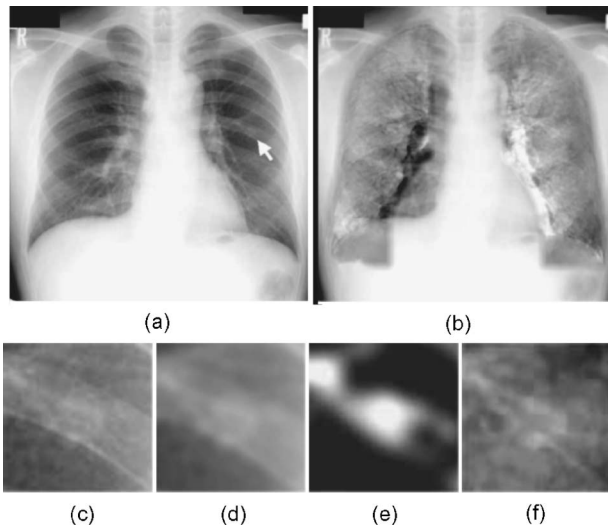
FIG. 5. Example of (a) original chest image including one lung nodule (arrow), (b) contralateral subtraction image obtained from original image, and segmented small ROI (50×50) obtained from (c) original image, (d) density-corrected original image, (e) nodule-enhanced image, and (f) contralateral subtraction image.
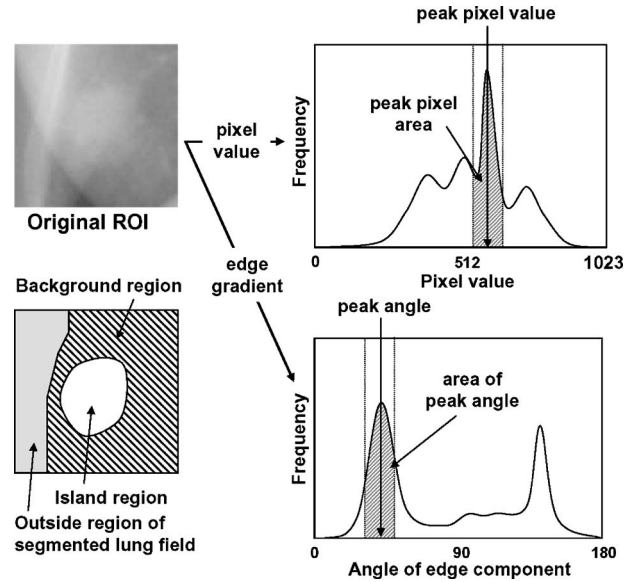

FIG. 6. Illustration of background image features which include the outline of island, background, and outside regions, the histogram of pixel values which were used for determining peak pixel value and peak pixel area, and the histogram of angular components of edge gradient for determining peak angle and area of peak angle. All image features were extracted from the small ROI (50×50 matrix size) of original image, center location of which is the same as the centroid of identified candidate.

ages. Finally, a total of 71 image features were employed for three ANNs in order to reduce the number of false-positive candidates.

Table II shows the list of image features extracted from

four different images used in our computerized scheme. The background features obtained from the background region, which was determined by the area between the nodule outline and the outer frame of a small ROI of original image. As illustrated in Fig. 6, background features included (1) the peak pixel value, (2) the peak pixel area ratio, which was determined by the ratio of the area for peak pixel values (bin of 10%) in the histogram to the entire area of the histogram, (3) the lung field area ratio, which was determined by the ratio of the segmented lung field area to the entire area of a small ROI, (4) the standard deviation of pixel values, (5) the average edge angle, which was determined by the average value of angular components of edge gradients, (6) the peak angle of the histogram for angular components of edge gradients (bin of 10°) within the range of posterior rib directions (i.e., 90° to 150° for the left peripheral region), (7) the ratio of the area of the peak angle for posterior ribs and the entire area of the histogram for angular components of edge gradients, (8) the peak angle for anterior ribs, and (9) the ratio of the area of the peak angle for anterior ribs and the entire area of the histogram.

When more than two nodule candidates were identified in adjacent locations (i.e., the distance between two centroids of nodule candidates was less than 16.0 mm), but were identified in the different localized search regions, in order to avoid the overlap of nodule candidates for one lesion, only one nodule candidate which had a larger effective diameter and/or a higher circularity was retained for the next step.

3. Sequential application of ANNs

In order to reduce the effect of overlapped ribs, before the use of three sequential ANNs, all nodule candidates were

TABLE II. List of 71 image features obtained at the initial identification (IN), and extracted from the original image (OR), density-trend correction (DC), nodule-enhanced image (ND), and contralateral subtraction (CL) images.

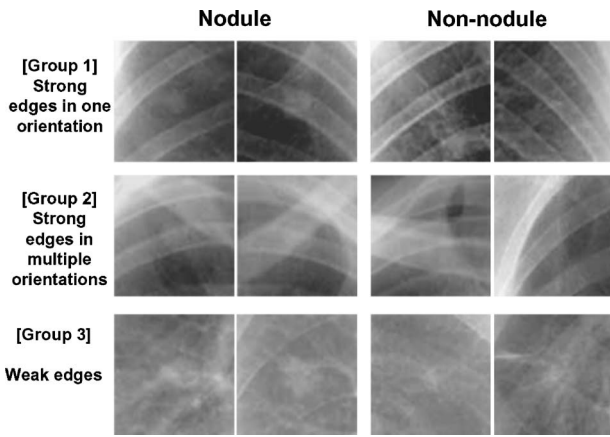|	IN	OR	DC	ND	CL
Geometric image features					
normalized horizontal position	o				
normalized vertical position	o				
horizontal distance from a mid-line	o				
effective diameter	o		o	o	
circularity	o		o	o	
irregularity	o		o	o	
Gray-level image features					
threshold value at detection	o				
average pixel value	o	o	o	o	o
standard deviation of pixel value		o	o	o	o
difference in pixel value between inside and outsize regions		o	o	o	o
contrast	o	o	o	o	o
Background image features					
peak pixel value		o			o
peak pixel area ratio		o			o
lung field area ratio		o			o
standard deviation of pixel value within ROI		o			o
average edge angle		o	o		
peak edge angle for posterior ribs		o	o		
peak edge ratio for posterior ribs		o	o		
peak edge angle for anterior ribs		o	o		
peak edge ratio for anterior ribs		o	o		
Edge gradient image features					
radial gradient index (RGI)		o	o	o	o
average radial gradient		o	o	o	o
standard deviation of radial gradient		o	o	o	o
average edge gradient		o	o	o	o
standard deviation of edge gradient		o	o	o	o
Other features					
sequential order in detection	o				
cross correlation for contralateral subtraction image					o
	10	18	17	12	14

FIG. 7. Example of lung nodule candidates (each of two actual nodules and two non-nodules) classified according to three rib-shape groups i.e., the ROI including a nodule candidate; [Group 1] strong edge in one orientation, [Group 2] strong edge in multiple orientations, and [Group 3] weak edges.

FIG. 8. Illustration of the overall training scheme for ANNs by use of the bootstrap method.

divided into three rib-shape groups as illustrated in Fig. 7 by use of three image features related to the background including ribs. We employed rib-shape group 1 for candidates that had a background structure of a strong edge peak due to posterior ribs only, group 2 for the candidates that had a background structure of strong peaks due to both posterior and anterior ribs, and group 3 for other candidates with weak edges. Three image features used for grouping were (5) the average edge angle, (7) the ratio of the area of the peak angle for posterior ribs to the entire area of the histogram, and (9) the corresponding ratio for anterior ribs, which are included in the background features described earlier. It is apparent in Fig. 7 that these three image features would be useful in classifying nodule candidates among the three rib-shape groups, thus allowing us to reduce the effect of background structure in the subsequent application of ANNs. Therefore, we determined all parameters of ANNs for each rib-shape group. All ANNs described in the following were trained and tested on each rib-shape group in each data set.

In order to determine parameters for the ANN such as the number of iterations; slope of sigmoid functions, learning rate, and threshold values for removing false positives, we divided 465 training cases randomly into 234 learning cases (254 nodules) and 231 tryout cases (246 nodules), where learning cases were used only for training ANNs and tryout cases only for testing ANNs. All of the ANNs were trained initially with the 234 learning cases, and were tested with the 231 tryout cases by use of a bootstrap technique.[32] The bootstrap technique is a resampling method, which allows generating a large number of "new" pseudocase sets from the original case set. We called each pseudocase set "BS case set," in this study. The bootstrap data points are a random sample of size n drawn *with* replacement from the original case set $(x_1, \ldots, x_n)$.[32] Therefore, the BS case set consists of members of the original case set, some appearing zero times, some appearing once, and some appearing more than once in the "new" BS case sets. Figure 8 illustrates the bootstrap method used in this study, where we used the number of true
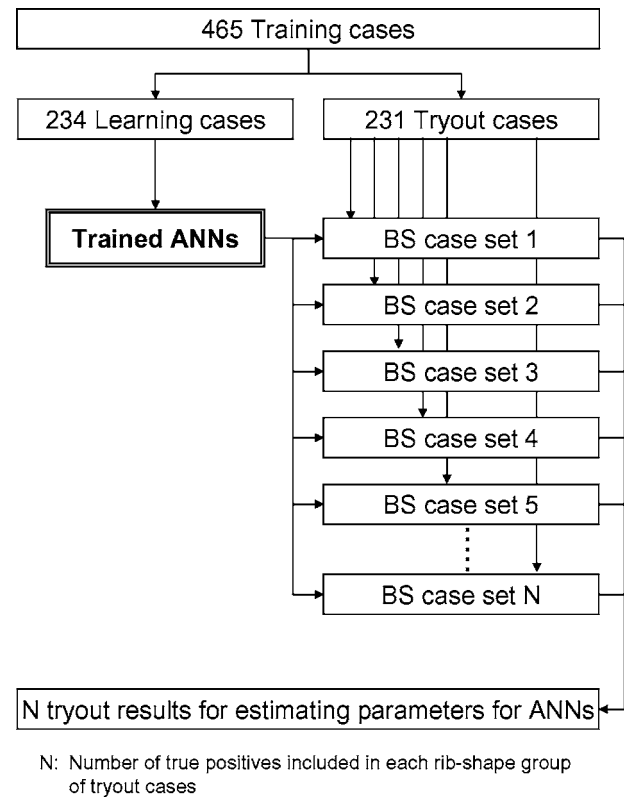
positives (i.e., lung nodules) in each rib-shape group of the original tryout cases as the same number of BS case sets, because we would like to keep the variation between BS case sets comparable to that of true positives.

In the first ANNs, we applied multiple simple ANNs, each of which included only two image features as the input data, in order to remove obvious false positives which were considered to be outliers in the two-dimensional space of any two image features, and might degrade the performance of the subsequent ANNs if not removed. Because we determined 41 image features (10 features obtained at initial detection, and 31 geometric, gray-level, and background features for original, density-trend-corrected original, and nodule-enhanced images), there are 820 combinations of any two image features as the input of the first ANNs. Each ANN for each of the 820 combinations of two image features was trained with the 234 learning cases by varying the number of iterations (100, 200, 300, 400, and 500) and the learning rates (0.02, 0.05, 0.10, and 0.20). We empirically employed one hidden layer with two hidden units and 1.0 for the slope of the sigmoid function. Once we trained ANNs with various numbers of iterations and the learning rate for the 820 combinations by use of the 234 learning cases, a number of BS case sets created from the 231 tryout cases by use of the bootstrap method were tested repeatedly with the same trained ANN. We monitored the effectiveness in the reduction of false positives by use of an index (I) in the tryout cases in order to determine a suitable number of iterations and a proper learning rate for each ANN, where I was deter-

mined by use of the number of false positives (N_{FP}) and the number of true positives (N_{TP}) removed by use of a cut-off threshold value of the ANN output (T), i.e.,

$$I = N_{FP}/(N_{TP} + 1). \qquad (3)$$

In order to determine the cut-off threshold value T for each ANN, we monitored the average of the lower 5% of all ANN output values for true-positive cases in the BS case sets. Then, the overall average (Ave) and its standard deviation (Std) for the average of minimum 5% ANN output values were obtained from all of the BS case sets. Finally, the cut-off threshold value T for each ANN was determined by

$$T = \text{Ave} - 2.58 \, \text{Std}, \qquad (4)$$

where the distribution of the minimum ANN output values was assumed to follow the central limit theorem,[33] and therefore the threshold value for each ANN was determined at 99.9% confidence in theory to include 95% of the ANN output obtained from the population of true positives. For each combination of two image features, one ANN parameter set (including the number of iterations and the learning rate) for obtaining the highest index value was determined automatically. Once we determined a suitable number of iterations, and the learning rate and the index for the 820 combinations, these combinations were ranked by use of the index value. In order to avoid overlaps of the role of each ANN for removing false positives, the 820 ANNs were applied to the 231 tryout cases sequentially until the index value became less than 1.0% of the number of false positives included in the tryout cases. For example, when one specific ANN which had higher index value could remove 3.6% of false positives with no reduction of true positives in training cases, this ANN was selected as one of the first ANNs. On the other hand, if the ANN could remove 3.8% of false positives with reduction of three true positives, this ANN was not selected. Therefore, the number of selected ANNs for the first ANNs was determined automatically and was independent from the data set used for training.

Figure 9 shows one result obtained from the first ANNs for tryout cases. Two image features selected for this ANN were the circularity of nodule candidates obtained from the nodule-enhanced image, and the difference in pixel values between the inside and outside regions of a nodule candidate obtained from the original image. The estimated cut-off value which was obtained by use of the bootstrap method could remove a number of obvious false-positive candidates with a small reduction of true positives in the tryout cases.

After removing obvious false positives in the first ANNs, we employed the second ANNs with four groups of image features as the input data for the four ANNs. These image feature groups included 10 image features in the initial identification, which were combined with (1) 12 nodule-enhanced image features, (2) 18 original image features, (3) 17 density-trend corrected original image features, and (4) 14 contralateral subtraction image features. We selected these four groups of image features empirically based on our knowledge. Each ANN for the four image feature groups was trained with the 234 learning cases by varying the number of
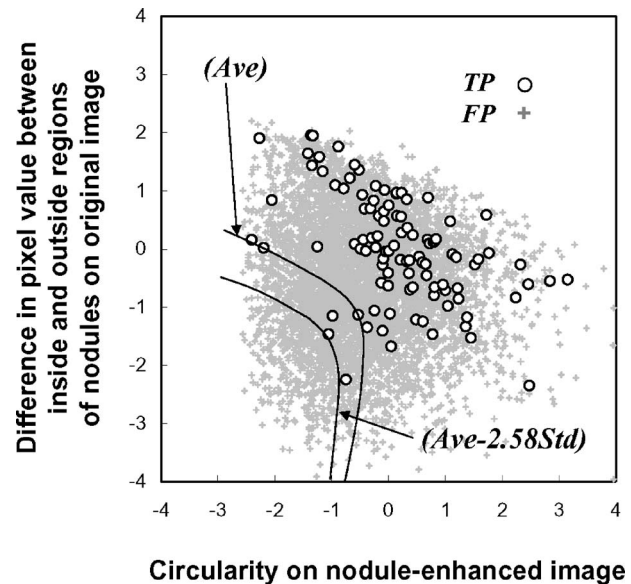

FIG. 9. Relationship between the circularity obtained from nodule-enhanced images and the difference in pixel value between inside and outside regions of nodule candidates obtained from original images. Boundary of threshold values (Ave-2.58Std) was determined by the bootstrap method for a single ANN with average minimum ANN outputs (Ave), and its standard deviation (Std).

iterations (1000, 2000, 3000, 4000, and 5000) and learning rates (0.02, 0.05, 0.10, and 0.20). We employed one hidden layer, one half of the number of input units as the number of hidden units, and 0.30 for the slope of the sigmoid function empirically. After we trained ANNs with various numbers of iterations and learning rates for the four image feature groups by the 234 learning cases, a number of BS case sets created from the 231 tryout cases by use of the bootstrap method were tested repeatedly with the same trained ANN. In this second ANNs, we monitored the average errors of ANN output in the BS case sets in order to determine a suitable number of iterations and learning rate for each image feature group. The average errors were calculated by the root mean square of differences between ANN output and teacher data (i.e., 0.90 for true positives and 0.10 for false positives). We determined the suitable ANN parameters when the average error in the BS case sets was minimized. We assumed that this method can reduce overtraining of ANNs.

The third ANN employed four inputs which corresponded to the output obtained from four ANNs with four image feature groups. The structure of third ANNs consisted of four input units with three hidden units of one hidden layer and one output unit. The slope of the sigmoid curve was 0.30 and the suitable number of iterations and the learning rate were determined by the same way as the method described for the second ANNs.

We tested 459 test cases (492 lung nodules) by use of all ANNs when their training was completed. All of the ANN parameters were determined automatically in advance by use of the 465 training cases, as described earlier. The performance of the computerized scheme for the detection of lung nodules was evaluated by use of free-response receiver op-

TABLE III. Numbers of test cases and nodules for four different data sets, which were selected randomly from the 924 cases, and the number of selected ANNs for the first ANNs determined by remaining training cases. Computer performance of the sensitivity and the number of false-positives per image were obtained at the steps of initial detection, the first ANNs, and the third ANN.

	Set 1	Set 2	Set 3	Set 4	Average
No. of images	459	465	460	464	462
No. of nodules	492	500	491	501	496
No. of ANNs selected for the first ANNs	7	5	9	7	7
Computer performance: Sensitivity (FPs/image)					
Initial detection	92.3 % (59.1)	92.4% (59.4)	92.3% (59.3)	93.2% (59.2)	92.5% (59.3)
First ANNs	90.9% (50.8)	90.2% (52.3)	90.4% (53.4)	91.6% (53.0)	90.8% (52.4)
Third ANN	70.1% (5.2)	70.0% (4.9)	70.5% (4.9)	69.9% (5.0)	70.1% (5.0)

erating characteristic (FROC) curves[34] which indicated the relationship between the sensitivity [%] of lung nodule detection and the number of false positives per image. In addition to the evaluation of the 459 test cases, we obtained the performance for the lung nodule detection by use of the 465 training cases in order to examine the difference between the two results.

The true-positive detection of the computerized scheme was determined when the distance between the centroid of a nodule candidate and the centroid of an actual lung nodule was less than 22.0 mm for the apical and peripheral regions or 24.0 mm for the hilum region.

III. RESULTS

Table III indicates the numbers of testing cases and of testing lung nodules included in four data sets and the number of rules selected in the first ANNs by use of training cases. The computer performance of the sensitivity and the number of false positives (FPs) are also shown in Table III, at the initial detection, for the first ANNs, and for the third ANNs. The average sensitivity of 92.45% and the average number of FPs of 59.25 per image at the step of initial detection were improved over those of our previous computerized scheme (sensitivity of 82.8% and 56.8 FPs per image), probably because subtle lung nodules of various sizes can be enhanced by use of an adaptive ARG filtering technique, and then detected by a multiple-thresholding technique. Figure 10 shows two examples of (a) the original nodule image and two processed images obtained from (b) our previous scheme by use of a difference-image technique[14] and (c) the ARG filtering technique. When a subtle lung nodule was projected on the interval between ribs as shown in Fig. 8, it was very difficult to isolate lung nodules from ribs by our previous scheme, because rib edges located on both sides of the lung nodule were enhanced more strongly than was the lung nodule. However, the ARG filtering technique can isolate such a lung nodule because this technique takes into account the orientation of edge gradients toward the center of the nodule.

The average number of selected image feature pairs for the first ANNs was 7. Because the first ANNs were used only for removing obvious false positives, a small number of two image feature pairs were likely to be selected conservatively without elimination of true positives, so that 11.6% of the initial FPs (average 6.9 of 59.3 FPs per image) were removed with a reduction of 1.7% in the sensitivity.

Figure 11 indicates the average FROC curves obtained from four sets of training and test cases. The average sensitivity and the average number of FPs per image obtained with this CAD scheme were 70.1% and 5.0 for the test cases and 70.4% and 4.2 for the training cases, respectively.

Figure 12 shows the relationship between the average sensitivity in the detection of lung nodules for four sets of testing cases and the size range of lung nodules detected, while the overall performance of the computerized scheme was retained with 70.4% sensitivity and 4.2 false positives per image. The computer performance was relatively high when the size of lung nodules was larger than 10.0 mm.

Figure 13 also shows the relationship between the average sensitivity in the detection of lung nodules for the four sets of test cases and the degree of subtlety of lung nodules at the same performance level used in Fig. 12. It should be noted

Original image   **Difference image by previous scheme**   **Nodule-enhanced image by ARG filter**
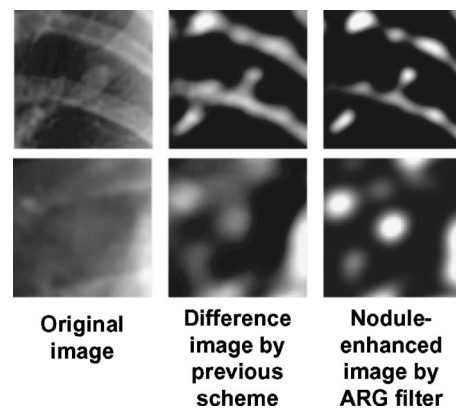
FIG. 10. Illustration of original nodule image and two different nodule-enhanced images which were obtained with our previous scheme by use of the difference-image technique and the ARG filtering technique.
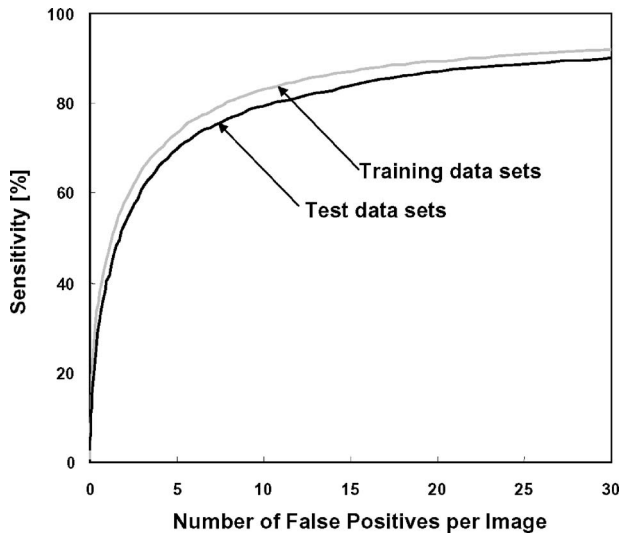
FIG. 11. Average FROC curves of the computerized scheme of lung nodule detection for four sets of training and test data sets.
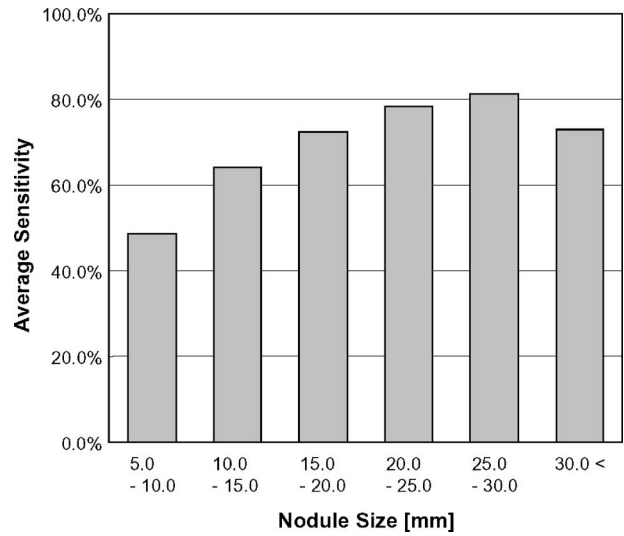

FIG. 12. Relationship between average sensitivity in the detection of lung nodules for four test cases and the size of lung nodules detected.

that the computer performance for the lung nodule detection was slightly better when the degree of subtlety for visual detection of lung nodules decreased.

Table IV shows the comparison of performances of the computerized scheme in the three shape groups at the initial and the final (third ANN) steps of identifications. The change in the sensitivities from the initial to the final identifications was comparable among the three shape groups. The change in the number of false-positives per image was different in the three shape groups. These results indicated that some false-positive candidates in the shape group 1 and 2 were distinguished effectively from true positives compared with false-positives in group 3.

IV. DISCUSSION

Tan *et al.*[35] reported that one of 500 chest radiographs demonstrates a lung nodule, and that 90% of these nodules are incidental radiologic findings detected unexpectedly in radiographs obtained for unrelated diagnostic workups. Their data might suggest that some lung nodules were likely to be overlooked by radiologists if they did not focus their attention on the detection of lung nodules. In fact, in the lawsuits,[36] failure to observe a lung cancer on a chest radiograph was considered a frequent cause of a missed diagnosis. The most important role of the CAD scheme for the detection of lung nodules would be to stimulate and prompt the radiologist's eyes and brain in order to avoid oversight of lung nodules.

Because the incidence of lung nodules on chest images is not very high (0.2% as described earlier), it is very difficult to collect a large number of lung nodule cases for research purposes. For example, when a chest radiologist interprets 100 chest images per day for 250 days in a year, it will take 20 years for meeting with 1000 lung nodule cases. Of course, radiologists can find many lung nodule images in teaching files, textbooks, and lectures; however, the majority of these lung nodules might be considered relatively obvious for visual detection by the radiologist. Therefore, the number of 924 chest images with 992 lung nodules may be considered as a sufficient number of cases in terms of the population of lung nodules which were located and visualized on the chest images.

TABLE IV. Number of identified lung nodules and sensitivities for 992 lung nodules and the number of false positives (FPs) per image for 924 images (data sets 1 and 2) at the initial and the final (third ANN) steps of detection for three shape groups.

		Total	Group 1	Group 2	Group 3
Initial detection	No. of nodules (sensitivity)	916 (92.3%)	201 (20.3%)	311 (31.4%)	404 (40.7%)
	No. of FPs per image	59.3	13.7	20.4	25.2
Third ANN	No. of nodules (sensitivity)	695 (70.1%)	147 (14.8%)	237 (23.9%)	311 (31.4%)
	No. of FPs per image	5.05	0.67	1.37	3.00
	Change in sensitivity from initial to third ANN	75.9%	73.1%	76.2%	77.0%
	Change in the number of FPs per image from initial to third ANN	8.5%	4.9%	6.7%	11.9%

The radial gradient index (RGI), which is a basic concept of the ARG filter technique, has been used in our laboratory for characterizing mass regions on mammography[37] and for a filtering technique on breast ultrasound.[38] Unlike the RGI and the RGI filtering technique which used a segmented lesion obtained by the region-growing technique, our ARG filter used a fixed circle for determining the filter output. A number of filtering techniques based on the radial component of local edge gradients toward the center of a region of interest, rather than the use of gray-scale information on a lung nodule, were developed in the past, such as the Fragmentary Window Filtering method reported by Mao *et al.*[20] in 1998 and the Convergence Index Filter reported by Wei *et al.*[39] in 2000. Although these two filtering methods used only a specified region such as a circular geometric pattern or parabolic lines toward the center, our method used radial components of edge gradients within the entire region of the circle. Therefore, our method would be more effective in the detection of lung nodules when the shape of a nodule is different from a circle and/or has irregular edges, because more information on localized edge gradients for a lung nodule can be included in our method.

We assumed that the improvement of sensitivity in the initial detection level was due to the application of the ARG filtering technique and the localized search method, for which all parameter settings took into account the information on anatomical classification results. The localized search method is more sensitive in the multiple thresholding procedure for detecting subtle lung nodules, compared with our previous method in which we used the histogram of the entire lung field for multiple thresholding.

The performance of the computerized scheme obtained in this study was not as high as that in previous reports,[17,18] probably because the number of cases used in this study was sufficiently large and thus the variation in lung nodule characteristics was ver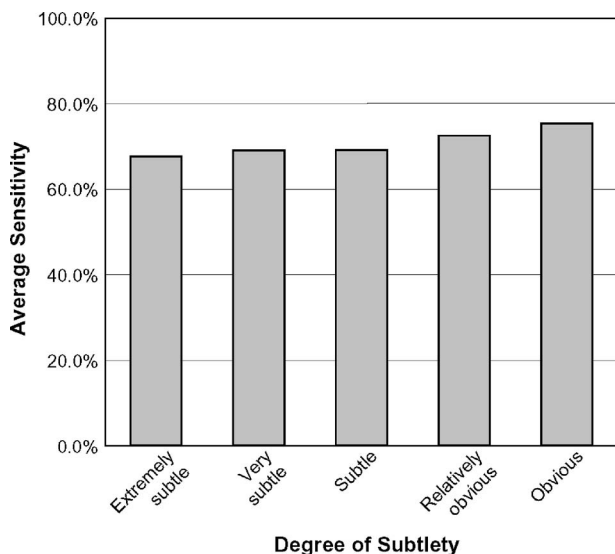y large. Therefore, we may expect that a comparable performance for the detection of lung nodules would be obtained in clinical situations, because the computerized scheme was trained for various types of lung nodules which would be considered close to those in the general population. In addition, when radiologists become familiar with computer-identified false-positive candidates which can be distinguished from actual nodules, some false positives remaining in our final results would be relatively easy to remove based on radiologists' subjective judgment.

From the relationship between the computer performance and the degree of subtlety for visual detection as shown in Fig. 12, it would be reasonable to assume that the difficulty in the detection of lung nodules by the computer was different from that in radiologists' interpretations. Therefore, improvement in radiologists' performance would be expected even if the performance of the computerized scheme for the detection of lung nodules was not very high; in fact, we demonstrated an improved performance in an observer performance study.[40]

V. CONCLUSION

We developed an advanced computerized scheme for the detection of lung nodules by incorporating a localized search method based on the anatomical classification and automated techniques for the parameter setting of three types of ANNs. The performance of this CAD scheme, which was trained by one half of 924 cases and then tested by the other half, provided improved detection of pulmonary nodules on chest radiographs.

ACKNOWLEDGMENTS

FIG. 13. Relationship between average sensitivity in the detection of lung nodules for four test cases and the degree of subtlety of lung nodules.

[a]Electronic mail: junji@uchicago.edu

[1]Cancer Facts & Figures 2004, The American Cancer Society, Inc.

[2]R. T. Heelan, B. J. Flehinger, M. R. Melamed, M. B. Zaman, W. B. Perchick, J. F. Caravelli, and N. Martini, "Non-small-cell lung cancer: Results of the New York screening program," Radiology **151**, 289–293 (1984).

[3]S. Sone, S. Takashima, F. Li, Z. Yang, T. Honda, Y. Maruyama, M. Hasegawa, T. Yamanda, K. Kubo, K. Hanamura, and K. Asakura, "Mass screening for lung cancer with mobile spiral computed tomography scanner," Lancet **351**, 1242–1245 (1998).

[4]J. K. Gohagan, P. M. Marcus, R. M. Fagerstrom, P. F. Pinsky, B. S.

Kramer, P. C. Prorok, S. Ascher, W. Bailey, B. Brewer, T. Church, D. Engelhard, M. Ford, M. Fouad, M. Freedman, E. Gelmann, D. Gierada, W. Hocking, S. Inampudi, B. Irons, C. C. Johnson, A. Jones, G. Kucera, P. Kvale, K. Lappe, W. Manor, A. Moore, H. Nath, S. Neff, M. Oken, M. Plunkett, H. Price, D. Reding, T. Riley, M. Schwartz, D. Spizarny, R. Yoffie, and C. Zylak, "Final results of the Lung Screening Study, a randomized feasibility study of spiral CT versus chest X-ray screening for lung cancer," Lung Cancer **47**, 9–15 (2005).

[5] C. I. Henschke, D. I. Mccauley, D. F. Yankelevitz, D. P. Naidich, G. McGuinness, O. S. Miettinen, D. M. Libby, M. W. Pasmantier, J. Koizumi, N. K. Altorki, and J. P. Smith, "Early Lung Cancer Action Project: Overall design and findings from baseline screening," Lancet **354**, 99–105 (1999).

[6] J. L. Mulshine and D. C. Sullivan, "Clinical practice. Lung cancer screening," N. Engl. J. Med. **352**, 2714–2720 (2005).

[7] UNSCEAR 2000. Report to the General Assembly, with Scientific Annexes, United Nations Scientific Committee on the Effects of Atomic Radiation, New York.

[8] E. J. Potchen and M. A. Bisesi, "When is it malpractice to miss lung cancer on chest radiographs?," Radiology **175**, 29–32 (1990).

[9] J. R. Muhm, W. E. Miller, R. S. Fontana, D. R. Sanderson, and M. A. Uhlenhopp, "Lung cancer detected during a screening program using four-month chest radiographs," Radiology **148**, 609–615 (1983).

[10] H. L. Kundel, C. F. Nodine, and E. A. Krupinski, "Computer-displayed eye position as a visual aid to pulmonary nodule interpretation," Invest. Radiol. **25**, 890–896 (1990).

[11] J. H. Austin, B. M. Romney, and L. S. Goldsmith, "Missed bronchogenic carcinoma: Radiographic findings in 27 patients with a potentially resectable lesion evident in retrospect," Radiology **182**, 115–122 (1992).

[12] K. Doi, "Overview on research and development of computer-aided diagnostic schemes," Semin Ultrasound CT MR **25**, 404–410 (2004).

[13] K. Doi, "Current status and future potential of computer-aided diagnosis in medical imaging," Br. J. Radiol. **78**, S3–S19 (2005).

[14] M. L. Giger, K. Doi, and H. MacMahon, "Image feature analysis and computer-aided diagnosis in digital radiography. 3. Automated detection of nodules in peripheral lung fields," Med. Phys. **15**, 158–166 (1988).

[15] Q. Li, S. Katsuragawa, and K. Doi, "Computer-aided diagnostic scheme for lung nodule detection in digital chest radiographs by use of a multiple-template matching technique," Med. Phys. **28**, 2070–2076 (2001).

[16] K. Suzuki, J. Shiraishi, H. Abe, H. MacMahon, and K. Doi, "False-positive reduction in computer-aided diagnostic scheme for detecting nodules in chest radiographs by means of massive training artificial neural network," Acad. Radiol. **12**, 191–201 (2005).

[17] X. W. Xu, K. Doi, T. Kobayashi, H. MacMahon, and M. L. Giger, "Development of an improved CAD scheme for automated detection of lung nodules in digital chest images," Med. Phys. **24**, 1395–1403 (1997).

[18] H. Suzuki, N. Inaoka, H. Takabatake, M. Mori, S. Sasaoka, H. Natori, and A. Suzuki, "Development of a computer-aided detection system for lung cancer diagnosis," Proc. SPIE **1652**, 567–571 (1992).

[19] S. C. Lo, M. T. Freedman, J. S. Lin, and S. K. Mun, "Automatic lung nodule detection using profile matching and back-propagation neural network techniques," J. Digit Imaging **6**, 48–54 (1993).

[20] F. Mao, W. Qian, J. Gaviria, and L. P. Clarke, "Fragmentary window filtering for multiscale lung nodule detection: Preliminary study," Acad. Radiol. **5**, 306–311 (1998).

[21] M. G. Penedo, M. J. Carreira, A. Mosquera, and D. Cabello, "Computer-aided diagnosis: A neural-network-based approach to lung nodule detection," IEEE Trans. Med. Imaging **17**, 872–880 (1998).

[22] M. Freedman, S. Lo, F. Lure, X. Xu, J. Lin, H. Zhao, T. Osicka, and R. Zhang, "Computer-aided detection of lung cancer on chest radiographs: Algorithm performance vs. radiologists' performance by size of cancer,"

Proc. SPIE **4319**, 150–159 (2001).

[23] S. Kakeda, J. Moriya, H. Sato, T. Aoki, H. Watanabe, H. Nakata, N. Oda, S. Katsuragawa, K. Yamamoto, and K. Doi, "Improved detection of lung nodules on chest radiographs using a commercial computer-aided diagnosis system," AJR, Am. J. Roentgenol. **182**, 505–510 (2004).

[24] J. Shiraishi, S. Katsuragawa, J. Ikezoe, T. Matsumoto, T. Kobayashi, K. Komatsu, M. Matsui, H. Fujita, Y. Kodera, and K. Doi, "Development of a digital image database for chest radiographs with and without a lung nodule: Receiver operating characteristic analysis of radiologists' detection of pulmonary nodules," AJR, Am. J. Roentgenol. **174**, 71–74 (2000).

[25] J. Shiraishi, H. Abe, R. Engelmann, and K. Doi, "Effect of high sensitivity in a computerized scheme for detecting extremely subtle solitary pulmonary nodules in chest radiographs: Observer performance study," Acad. Radiol. **10**, 1302–1311 (2003).

[26] Q. Li, S. Katsuragawa, and K. Doi, "Improved contralateral subtraction images by use of elastic matching technique," Med. Phys. **27**, 1934–1942 (2000).

[27] X. W. Xu and K. Doi, "Image feature analysis for computer-aided diagnosis: Accurate determination of ribcage boundary in chest radiographs," Med. Phys. **22**, 617–626 (1995).

[28] X. W. Xu and K. Doi, "Image feature analysis for computer-aided diagnosis: Detection of right and left hemidiaphragm edges and delineation of lung field in chest radiographs," Med. Phys. **23**, 1613–1624 (1996).

[29] S. Katsuragawa, K. Doi, and H. MacMahon, "Image feature analysis and computer-aided diagnosis in digital radiography: Detection and characterization of interstitial lung disease in digital chest radiographs," Med. Phys. **15**, 311–319 (1988).

[30] M. L. Giger, K. Doi, H. MacMahon, C. E. Metz, and F. F. Yin, "Pulmonary nodules: Computer-aided detection in digital chest images," Radiology **10**, 41–51 (1990).

[31] T. Matsumoto, H. Yoshimura, K. Doi, M. L. Giger, A. Kano, H. MacMahon, K. Abe, and S. M. Montner, "Image feature analysis of false-positive diagnoses produced by automated detection of lung nodules," Invest. Radiol. **27**, 587–597 (1992).

[32] B. Efron and R. J. Tibshirani, *An Introduction to the Bootstrap* (Chapman & Hall, New York, 1993).

[33] A. Papoulis, *Probability, Random Variables, and Stochastic Processes* (McGraw-Hill, New York, 1991).

[34] D. P. Chakraborty, "Maximum likelihood analysis of free-response receiver operating characteristic (FROC) data," Med. Phys. **16**, 561–568 (1989).

[35] B. B. Tan, K. R. Flaherty, E. A. Kazerooni, and M. D. Iannettoni, "The solitary pulmonary nodule," Chest **123**, 89S-96S (2003).

[36] M. M. Hamer, F. Morlock, H. T. Foley, and P. R. Ros, "Medical malpractice in diagnostic radiology: Claims, compensation, and patient injury," Radiology **164**, 263–266 (1987).

[37] Z. Huo, M. L. Giger, C. J. Vyborny, U. Bick, P. Lu, D. E. Wolverton, and R. A. Schmidt, "Analysis of spiculation in the computerized classification of mammographic masses," Med. Phys. **22**, 1569–1579 (1995).

[38] K. Drukker, M. L. Giger, K. Horsch, M. A. Kupinski, C. J. Vyborny, and E. B. Mendelson, "Computerized lesion detection on breast ultrasound," Med. Phys. **29**, 1438–1446 (2002).

[39] J. Wei, H. Hagihara, and H. Kobatake, "Detection of cancerous tumors on chest X-ray images—candidate detection filter and its evaluation," *International Conference on Image Processing (ICIP'99)* (IEEE Computer Society Press, Los Alamitos, CA, 1999).

[40] T. Matsumoto, H. Yoshimura, M. L. Giger, K. Doi, H. MacMahon, S. M. Montner, and T. Nakanishi, "Potential usefulness of computerized nodule detection in screening programs for lung cancer," Invest. Radiol. **27**, 471–475 (1992).